Complex-amplitude metasurface-based orbital angular momentum holography in momentum space

Haoran Ren[1, *, †], Xinyuan Fang[2, †], Jaehyuck Jang[3, †], Johannes Bürger [1], Junsuk Rho[3, 4, *] and Stefan A. Maier[1, 5, *]

[1] Chair in Hybrid Nanosystems, Nanoinstitute Munich, Faculty of Physics, Ludwig-Maximilians-Universität München, München, 80539, Germany

[2] Centre for Artificial-Intelligence Nanophotonics, School of Optical-Electrical and Computer Engineering, University of Shanghai for Science and Technology, Shanghai, 200093, China

[3] Department of Chemical Engineering, Pohang University of Science and Technology (POSTECH), Pohang, 37673, Republic of Korea

[4] Department of Mechanical Engineering, Pohang University of Science and Technology (POSTECH), Pohang, 37673, Republic of Korea

[5] Department of Physics, Imperial College London, London SW7 2AZ, United Kingdom

Email: Haoran.Ren@physik.uni-muenchen.de; jsrho@postech.ac.kr; Stefan.Maier@physik.uni-muenchen.de

† These authors contributed equally to this work

Abstract

Digital optical holograms can achieve nanometer-scale resolution thanks to recent advances in metasurface technologies. This has raised hopes for applications in data encryption, data storage, information processing and displays. However, the hologram bandwidth has remained too low for any practical use. To overcome this limitation, information can be stored in the orbital angular momentum (OAM) of light, as this degree of freedom has an unbounded set of orthogonal helical modes that could function as information channels. Thus far, OAM holography has been achieved using phase-only metasurfaces, which however are marred by channels crosstalk. As a result, multiplex information from only 4 channels has been demonstrated. Here we demonstrate an OAM holography technology that is capable of multiplexing up to 200 independent OAM channels. This is achieved by designing a complex-amplitude metasurface in momentum-space capable of complete and independent amplitude and phase manipulation. Information is then extracted by Fourier transform using different OAM modes of light, allowing lensless reconstruction and holographic videos being displayed. Our metasurface can be 3D printed in a polymer matrix on SiO_2 for large-area fabrication.

Optical holography is a promising technology for realistic 3D displays[1, 2], optical encryption[3, 4], data storage[5], and artificial intelligence[6]. Recent advances in metasurface-based flat optics[7-9] have opened up the possibility of using ultrathin metasurface for hologram digitalization[10-16], towards high-capacity holographic technology. Development of high-bandwidth metasurface holograms is essential for optically addressable holographic video displays with potentially ultrafast switching of image frames. Optical multiplexing uses physical properties of light to carry independent holographic image channels, thus improving the bandwidth of a metasurface hologram. In this context, spatially interleaved metasurfaces consisting of multiple sets of polarization- and wavelength-sensitive meta-atoms have been designed for holographic multiplexing[17-20], albeit with strong crosstalk and limited bandwidth. Alternatively, the anisotropic property of a single meta-atom has been tailored for polarization- and angle-sensitive optical responses[21-23], although the availability of distinct optical modes for multiplexing is rather limited and bandwidth remains low.

Orbital angular momentum (OAM) manifests itself as a twisted wavefront of light, and has emerged as a novel way to boost information capacity due to its physically unbounded set of orthogonal helical modes[24-28]. Through appropriate spatial-frequency sampling of a digital hologram in momentum space, the OAM property of an incident light can be preserved for selectively addressing OAM-dependent holographic images[4, 29]. However, such phase-only metasurface holograms prohibit an exact convolution between a complex-amplitude image channel and an OAM helical wavefront. As a result, the linear superposition principle is broken and image multiplexing suffers from strong crosstalk. Thus, this approach restricts the maximum multiplexing channels to four[29]. Even though complex-amplitude metasurfaces have recently been

developed to perform Fresnel holography based on wave propagation theory[10, 30-32], Fresnel holograms fail to implement OAM holography as they are not designed for momentum-space image reconstruction. In addition, metasurface fabrication is costly, leading to planar metasurface holograms designs with limited degrees of freedom, which require a bulky microscope for image reconstruction.

Here we show the design and 3D laser manufacturing of a large-scale complex-amplitude metasurface for ultrahigh-dimensional OAM-multiplexing holography in momentum space. Such high-bandwidth metasurface holograms allow us to demonstrate lensless reconstruction of up to 200 of orthogonal image channels encoded within an OAM signature, leading to optically-addressable holographic video displays without involving any spatial scanning approach[33-35]. Without loss of generality, we select OAM modes with helical mode indices (l) ranging from -50 to 50 (Fig. 1a) to be sequentially incident on a large-scale complex-amplitude OAM-multiplexing metasurface hologram (COMH) (Fig. 1b) for addressing OAM-dependent orthogonal image frames (Fig. 1c), with two distinct holographic videos being simultaneously reconstructed in momentum space. The independent reconstruction of holographic videos in two different planes suggests that our approach can be applied for 3D holography. Unlike the conventional metasurfaces with restricted degrees of freedom in a 2D plane, we introduce the design and laser-based printing of a 3D metasurface, in which the height (H) and in-plane rotation (θ) of a birefringent polymer nanopillar are employed to independently control the amplitude and phase responses of transmitted light, respectively (Fig. 1b).

Design principle

Mathematically, OAM-multiplexing holography can be represented as superposition of complex-amplitude fields of different image channels encoded with distinctive OAM modes in the hologram plane: $E^{mul} = \sum_{j=1}^{M} A_j e^{i\emptyset_j} e^{il_j\varphi}$, wherein A_j and $\emptyset_j$ stand for the amplitude and phase information of each image channel, respectively; $l_j \in \mathbb{Z}$ and φ represent the helical mode index and azimuthal angle, respectively, and *M* denotes the total number of multiplexing channels. Since the complex-amplitude hologram is Fourier-based (Supplementary Note 1), its reconstructed optical fields in momentum space can be represented as $\mathcal{F}(E^{mul}) = \sum_{j=1}^{M} \mathcal{F}(A_j) \otimes \mathcal{F}(e^{i\emptyset_j}) \otimes \mathcal{F}(e^{il_j\varphi})$, where $\mathcal{F}$ denotes the Fourier transform (FT) operator, expressing multiplexing results as the superposition of a convolution of the amplitude (A_j), phase ($\emptyset_j$), and encoded OAM (l_j) information of each image channel. It is obvious to see that the amplitude of each image channel can be individually controlled, allowing the adjustment of image frame intensity essential for high-quality holographic video displays. On the other hand, a phase-only OAM-multiplexing hologram can be described as an argument result: $P^{mul} = \arg\left[\sum_{i=1}^{M} e^{i\emptyset_i'} e^{il_i\varphi}\right]$, wherein $\emptyset_i'$ denotes an iteratively-retrieved phase-only hologram for each image channel. The reconstructed optical fields in momentum space can thus be represented as $\mathcal{F}(P^{mul}) = \mathcal{F}\left\{\arg\left[\sum_{i=1}^{M} e^{i\emptyset_i'} e^{il_i\varphi}\right]\right\}$, indicating that the amplitude information of each image channel is completely lost, which degrades the reconstruction quality by making the image channel intensity non-uniform (fig. S1). Moreover, neglecting the amplitude information results in strong crosstalk[34], due to the non-exact reproduction of the convolution relationship as compared to the complex-amplitude multiplexing results. Specifically, we present a general multiplexing case by superposing two blazed phase gratings in the hologram plane. The resulting multiplexing fields in

the image plane of a phase-only hologram exhibit significant deviations from the ones of a complex-amplitude hologram (fig. S2).

The design principle of a complex-amplitude hologram for OAM holography is illustrated in Figure 2. To achieve OAM holography, we developed an OAM diffuser array that consists of an OAM-dependent sampling array and a random phase function, performing the spatial-frequency sampling in momentum space (Fig. 2a). As such, the inverse FT of a sampled target image gives rise to a complex-amplitude hologram with a discrete spatial-frequency content. In each holographic image channel, a specific OAM helical phase and a FT lens were added to the phase information of the complex-amplitude hologram, leading to strong OAM selectivity at a given image plane (fig. S3). According to diffraction theory, the size of OAM pixels in the image space can be determined from both the helical mode index (l) at a given wavelength and the effective numerical aperture of the Fourier hologram with respect to a specific image plane (Supplementary Note 2). As a result, we numerically characterized the size of diffraction-limited OAM pixels at different planes as a function of the helical mode index, which explicitly gives rise to both the maximal multiplexing channel number and the upper resolution limit of the holographic image (Fig. 2b). The trade-off between the highest OAM helical mode index and the resolution of the OAM-dependent holographic images sets up an upper limit of the maximum multiplexing channel number when a certain image resolution is specifically required. To further improve the image resolution, the effective numerical aperture of the Fourier hologram should be increased by either enlarging the hologram size or reducing the reconstruction distance (figs. S4 and S5).

Notably, the random phase of an OAM diffuser array plays a key enabling role in the

digitalization of a complex-amplitude hologram (Fig. 2c). More specifically, the broad spatial-frequency content of a random phase function acts as a convolution kernel to diffuse the amplitude of a Fourier hologram, capable of flattening the large amplitude variation present in a typical complex-valued Fourier hologram (fig. S6). To quantify the effect of the random phase on digitalization, we numerically calculated the coefficient of variation as a function of OAM-multiplexing channel number (Methods). Without the OAM diffuser array, the coefficient of variation in the amplitude part of a Fourier hologram is nearly 300% for a typical set of images and increases with the multiplexing channel number. This results in about 90% area of the Fourier hologram having normalized amplitudes smaller than 0.05. This sets a fundamental barrier to digitalize a Fourier hologram due to the loss of phase information and low transmission efficiency (less than 2.5‰) in that area. After applying the OAM diffuser array, the coefficient of variation is reduced below 100% and kept nearly constant by increasing the multiplexing channel number (Fig. 2d). It is worth noting that the random phase of an OAM diffuser array can also eliminate the coherence of image channels and further suppress multiplexing crosstalk in addition to the OAM orthogonality. We show that the coherence of two images, defined as normalized inner vector product of image pixels[34], can be reduced by one order of magnitude when different random phase functions are added to individual images (Fig. 2d and fig. S7).

Complex-amplitude hologram-based multiplexing holography

The physical mechanism of complex-amplitude-based OAM-multiplexing holography and its application for holographic video displays are demonstrated in Figure 3. To create a complex-amplitude OAM-multiplexing hologram, we extracted high-resolution image frames from the

original “football” and “basketball” videos with a frame rate of 25 fps (frames per second). Each image frame was further sampled by an OAM diffuser array with the random phase function differing from image to image (Fig. 3a). Thereafter, a complex-amplitude hologram for each image frame was obtained by performing the inverse FT of the sampled image frame. To obtain OAM selectivity, an OAM helical phase function was added to the phase information of each complex-amplitude hologram. In this case, owing to the OAM conservation, only a given OAM mode with an inverse helical mode index can recover the fundamental spatial mode with a point-like intensity distribution in each pixel, leading to distinctive reconstruction of the holographic image. We transferred the time-sequence information of the original videos into the OAM degree of freedom, as such, it allows the use of optical OAM beams to dynamically address OAM-dependent image frames for holographic video displays.

To illustrate the potential of our approach for 3D holographic video displays, the “football” and “basketball” videos were designed at two image planes by further adding different FT lens functions to the phase information of the complex-amplitude holograms. Consequently, a high-resolution complex-amplitude OAM-multiplexing hologram with 10000 by 10000 pixels was numerically designed (Fig. 3b) and characterized for an all-optical holographic video display (Fig. 3c). We show that high-quality “football” and “basketball” videos, each of which contains 100 image frames at 260 pixels per inch, can be simultaneously reconstructed at two different planes by sequentially exposing the complex-amplitude OAM-multiplexing hologram with an OAM beam with helical mode indices ranging from -50 to 50 at an interval of one (Movies S1 and S2, Fig. 3c). It should be pointed out that the numerical design of the complex-amplitude OAM-

multiplexing hologram costs two-orders of magnitude less calculation time than the case of a phase-only-based multiplexing hologram that relies on an iterative algorithm (fig. S8).

Design and fabrication of a complex-amplitude metasurface

We demonstrate the design and optimization of a novel 3D metasurface for the complete and independent manipulation of both amplitude and phase of transmitted light. For this purpose, a low refractive index (n=1.52) polymer-based rectangular nanopillar with an aspect ratio of up to 15 was used as our meta-atom (Fig. 4a). Such a high-aspect-ratio nanopillar can be designed to exhibit strong birefringence manifested by converting the polarization states of transmitted light (inset of Fig. 4a), laying the physical foundation of the geometric phase response based on the in-plane rotation angle (θ)[37]. Specifically, according to Jones matrix calculation a local geometric phase ($\emptyset$=-2θ) can be introduced for cross circular polarization by a simple in-plane rotation of the nanopillar (Supplementary Note 3). As such, the amplitude and initial phase retardation of the cross polarization of a light beam transmitted from a polymer nanopillar were numerically simulated with periodic boundary conditions as a function of nanopillar height (H) and length (L) (Fig. 4b and 4c, Methods). To reduce the parameter space, we fixed the pitch distance of nanopillars to 1.25 μm and the width (W)-to-length (L) ratio to 0.5. The results indicate that the cross-polarization efficiency can be modulated by H, and hence independent amplitude and phase modulation can be achieved from the out-of-plane height (H) and the in-plane rotation angle (θ) degrees of freedom of a 3D meta-atom, respectively.

In our experiment, we used 3D laser printing technology based on two-photon polymerization induced by a femtosecond laser to fabricate 3D metasurface samples. To simplify

our design for laser printing, we selected nanopillars of the same transverse size (W=390 nm and L=780 nm) and different heights in a small range from 3.45 μm to 4.32 μm to reduce the shadowing effect. Thereby 8-level amplitude modulation at a wavelength of 633 nm was realized (dashed line in Fig. 4b, Methods). It should be noted that the absolute amplitude of cross polarization does not influence the accuracy of digitalization of a complex-amplitude metasurface, but it could affect the overall diffraction efficiency of the metasurface. For even higher diffraction efficiency, we can further reduce the pitch distance of nanopillars and choose nanopillars of different transverse dimensions to provide higher absolute amplitude values (fig. S9). To experimentally verify the amplitude modulation, we fabricated blazed phase gratings of different heights (nanopillars in each grating sample have a uniform height), the characterization results of which show great consistency with the simulation (Fig. 4d and fig. S10). Notably, to properly digitalize a complex-amplitude metasurface, the initial phase (dashed line in Fig. 4c) induced by nanopillars of different heights should be compensated by the geometric phase. As a consequence, our designed and fabricated 3D meta-atoms can access arbitrary points in the complex plane (Fig. 4e), leading to a 64-level complex-amplitude metasurface that consists of polymer nanopillars with 8 different heights having 8 different in-plane rotation angles (Fig. 4f).

Characterization of metasurface multiplexing holography

To experimentally demonstrate ultrahigh-dimensional OAM-multiplexing holography, we fabricated a large-scale COMH (2.5 mm by 2.5 mm) consisting of 2000 by 2000 pixels (Fig. 5a). The inset of Fig. 5a shows an optical image of the fabricated COMH, while the top- and oblique-view scanning electron microscopy images of enlarged areas in the COMH are presented in Figs.

5b and 5c, respectively. Even though a small tapering angle was observed in our fabricated polymer nanopillars due to the ellipsoid shape of the diffraction-limited focal voxel-the fundamental building block in the 3D laser printing-we show that the discrepancy in both amplitude and phase modulation between nanopillars with a straight and tapered top is small (fig. S11). As such, this tapering effect in the fabricated polymer nanopillars exhibits a negligible influence on the metasurface performance. The optical setup for the lensless reconstruction of OAM-dependent holographic image frames is given in fig. S12, in which a spatial light modulator was used to dynamically generate different OAM beams. Two holographic videos of a "rotating triangle" and a "winding spiral" consisting of 60 image frames in total were numerically designed to carry an OAM signature and to be located at a distance of 20 mm and 30 mm from the hologram, respectively. To completely capture holographic image frames by a charge-coupled detector, which has a limited aperture size, the physical size of image frames was set as 7 mm by 7 mm. Consequently, OAM beams with helical mode indices ranging from -30 to 30 at an interval of two were sequentially directed onto the COMH, leading to the lensless reconstruction of "rotating triangle" (fig. S13, Movie S3) and "winding spiral" holographic videos (fig. S14, Movie S4), each of which consists of 30 OAM-dependent holographic image frames (Fig. 5d). To further improve the OAM selectivity, a fundamental mode filtering aperture array was added during post-processing to rule out the reconstructed high-order OAM pixels with doughnut-shaped intensity distributions (fig. S15). The noticeable image resolution reduction as compared to our simulation results in Figure 3 is mainly due to the difference in the pixel number (10,000 by 10,000 vs. 2,000 by 2,000) of the simulated and fabricated OAM-multiplexing holograms. In the future, ultrahigh-

throughput 3D laser printing techniques[38] may be used to print centimetre-scale complex-amplitude metasurface holograms leading to smaller OAM pixels and hence higher image resolution (figs. S4 and S5).

In addition, we show that our demonstration can be used for the design of an OAM-encrypted multiplexing hologram for ultra-security holographic encryption (fig. S17). For this purpose, we numerically design and characterize a novel OAM-encrypted multiplexing hologram through incorporating a randomized image encoding scheme. Specifically, we present a case in which a QR code is randomly distributed into a set of secret shares which are further encoded with 30 distinctive OAM modes, giving rise to the design of an ultra-secure OAM-encrypted multiplexing hologram (fig. S17). In the decryption process, the complete QR code and its information can be successfully extracted (read-out) only when the 30 correct OAM modes are simultaneously provided, while all the other cases capable of reconstructing partial QR codes fail to recognize the contained information. Our demonstrated OAM-based holographic encryption can potentially expand the code library from a 6-bit polarization- and wavelength-encoded hologram[39] to a 200-bit OAM-encoded hologram.

Conclusions

We have demonstrated the design of a complex-amplitude hologram for ultrahigh-dimensional multiplexing of holographic images in momentum space. We believe that our demonstrated OAM-multiplexing holography based on flat meta-optics provides a substantial advance towards powerful holographic memory devices, which can be used for ultrafast switching holographic video displays and ultra-secure optical encryption. To digitalize a complex-amplitude Fourier

hologram, we have introduced an OAM diffuser array with random phase capable of scaling down the amplitude variation as well as eliminating the coherence of holographic image channels. As such, OAM beams with a large range of helical mode indices from -50 to 50 impinge on the complex-amplitude hologram and sequentially address 200 OAM-dependent orthogonal holographic image frames, allowing an all-optical holographic video display without the need of any spatial scanning approaches[33-35]. In our experiment, a spatial light modulator (SLM) was used to generate different OAM modes, which sets up the theoretical upper limit of the OAM mode of around 500 for a SLM for a typical pixel size of 8 μm. However, this practical OAM mode index constraint can be relaxed when the resolution of a SLM or other diffractive optical elements is increased. Our simulation suggests that increasing the device resolution to 500 nm could significantly boost the maximum OAM helical mode index up to 15000 (fig. S16).

In contrast to conventional holographic memory devices made from volume holograms that rely on linear momentum selectivity (propagation direction and wavelength of light) via Bragg diffraction, our concept offers the fundamentally different approach of storing different digital images into the OAM degree of freedom of light. Notably, the OAM-multiplexing hologram is a computer-generated hologram in nature and can be digitalized by a planar complex-amplitude metasurface, whereas volume holograms inevitably use a thick storage medium to record the multiplexed optical images. Moreover, due to the theoretically unlimited orthogonal OAM modes of light in momentum space, massive independent holographic image channels can be stored and retrieved without scanning either the propagation direction or the wavelength of light.

In addition, we have presented a novel design and nanofabrication of a 3D metasurface

through exploiting the height degree of freedom of a polymer-based nanopillar, offering independent and complete manipulation of both amplitude and phase of transmitted light. To experimentally digitalize a complex-amplitude metasurface, we have employed high-resolution and cost-effective laser printing technology, leading to the fabrication of a large-scale (2.5 mm by 2.5 mm) COMH that comprises 2000 by 2000 pixels. Consequently, we have experimentally achieved the lensless reconstruction of two holographic videos at different image planes, which holds great promise for future realistic 3D holographic video display. It is worth mentioning that combining the COMH with vortex microlasers [40-42] could allow a dynamic holographic video display with potentially ultrafast switching speeds of 1 to 1.5 picoseconds per frame. It could also stimulate new applications in related fields such as deep-learning microscopy[43], optical trapping[44], smart head-up display, and wearable devices for augmented reality.

References

1. Downing, E., Hesselink, L., Ralston, J. & Macfarlane, R. A three-color, solid-state, three-dimensional display. *Science* **273**, 1185-1189 (1996).
2. Tay, S. *et al*. An updatable holographic three-dimensional display. *Nature* **451**, 694-698 (2008).
3. Li, J. *et al*. Addressable metasurfaces for dynamic holography and optical information encryption. *Sci. Adv.* **4**, eaar6768 (2018).
4. Fang, X., Ren, H. & Gu, M. Orbital angular momentum holography for high-security encryption. *Nat. Photonics* **14**, 102-108 (2020).
5. Heanue, J. F., Bashaw, M. C., & Hesselink, L. Volume holographic storage and retrieval of digital data. *Science* **265**, 749-752 (1994).

6. Lin, X. *et al*. All-optical machine learning using diffractive deep neural networks. *Science* **361**, 1004-1008 (2018).
7. Yu, N. *et al*. Light propagation with phase discontinuities: Generalized laws of reflection and refraction. *Science* **334**, 333-337 (2011).
8. Lin, D., Fan, P., Hasman, E. & Brongersma, M. L. Dielectric gradient metasurface optical elements. *Science* **345**, 298-302 (2014).
9. Arbabi, A., Horie, Y., Bagheri, M. & Faraon, A. Dielectric metasurfaces for complete control of phase and polarization with subwavelength spatial resolution and high transmission. *Nat. Nanotechnol.* **10**, 937–943 (2015).
10. Ni, X., Kildishev, A. V. & Shalaev, V. M. Metasurface holograms for visible light. *Nat. Commun.* **4**, 2807 (2013).
11. Huang, L. *et al*. Three-dimensional optical holography using a plasmonic metasurface. *Nat. Commun.* **4**, 2808 (2013).
12. Zheng, G. *et al*. Metasurface holograms reaching 80% efficiency. *Nat. Nanotechnol.* **10**, 308-312 (2015).
13. Wang, L. *et al*. Grayscale transparent metasurface holograms. *Optica* **3**, 1504–1505 (2016).
14. Hu, Y. *et al*. 3D-integrated metasurfaces for full-colour holography. *Light Sci. Appl.* **8**, 86 (2019).
15. Chen, W. T. *et al*. High-efficiency broadband meta-hologram with polarization-controlled dual images. *Nano Lett.* **14**, 225-230 (2014).
16. Wang, H. *et al*. Ultrathin planar cavity metasurfaces. *Small* **14**, 1703920 (2018)

17. Montelongo, Y. *et al*. Plasmonic nanoparticle scattering for color holograms. *Proc. Natl. Acad. Sci. U.S.A* **111**, 12679-12683 (2014).

18. Wen, D. *et al*. Helicity multiplexed broadband metasurface holograms. *Nat. Commun.* **6**, 8241 (2015).

19. Huang, Y. *et al*. Aluminium plasmonic multicolour meta-hologram. *Nano Lett.* **15**, 3122-3127 (2015).

20. Wang, B. *et al*. Visible-frequency dielectric metasurfaces for multiwavelength achromatic and highly dispersive holograms. *Nano Lett.* **16**, 5235-5240 (2016).

21. Kamali, S. M. *et al*. Angle-multiplexed metasurfaces: encoding independent wavefronts in a single metasurface under different illumination angles. *Phys. Rev. X* **7**, 041056 (2017).

22. Mueller, J. P. B., Rubin, N. A., Devlin, R. C., Groever, B. & Capasso, F. Metasurface polarization optics: independent phase control of arbitrary orthogonal states of polarization. *Phys. Rev. Lett.* **118**, 113901 (2017).

23. Zhao, R. *et al*. Multichannel vectorial holographic display and encryption. *Light Sci. Appl.* **7**, 95 (2018).

24. Wang, J. *et al*. Terabit free-space data transmission employing orbital angular momentum multiplexing. *Nat. Photonics* **6**, 488-496 (2012).

25. Bozinovic, N. *et al*. Terabit-scale orbital angular momentum mode division multiplexing in fibers. *Science* **340**, 1545-1548 (2013).

26. Ren, H., Li, X., Zhang, Q. & Gu, M. On-chip noninterference angular momentum multiplexing of broadband light. *Science* **352**, 805-809 (2016).

27. Mair, A., Vaziri, A., Weihs, G. & Zeilinger, A. Entanglement of the orbital angular momentum states of photons. *Nature* **412**, 313-316 (2001).

28. Fickler, R. *et al*. Quantum entanglement of high angular momenta. *Science* **338**, 640-643 (2012).

29. Ren, H. *et al*. Metasurface orbital angular momentum holography. *Nat. Commun.* **10**, 2986 (2019).

30. Lee, G. *et al*. Complete amplitude and phase control of light using broadband holographic metasurfaces. *Nanoscale* **10**, 4237-4245 (2018).

31. Overvig, A. C. *et al*. Dielectric metasurfaces for complete and independent control of the optical amplitude and phase. *Light Sci. Appl.* **8**, 95 (2018).

32. Deng, Z. *et al*. Full-color complex-amplitude vectorial holograms based on multi-freedom metasurfaces. *Adv. Funct. Mater.* **30**, 1910610 (2020).

33. Smalley, D. E., Smithwick, Q. Y. J., Bove, V. M., Barabas, J. & Jolly, S. Anisotropic leaky-mode modulator for holographic video displays. *Nature* **498**, 313-317 (2013).

34. Smalley, D. E. *et al*. A photophoretic-trap volumetric display. *Nature* **553**, 486-490 (2018).

35. Hirayama, R., Plasencia, D. M., Masuda, N. & Subramanian, S. A volumetric display for visual, tactile and audio presentation using acoustic trapping. *Nature* **575**, 320-323 (2019).

36. Makey, G. *et al*. Breaking crosstalk limits to dynamic holography using orthogonality of high-dimensional random vectors. *Nat. Photonics* **13**, 251-256 (2019).

37. Bomzon, Z., Biener, G., Kleiner, V. & Hasman, E. Space-variant Pancharatnam–Berry phase optical elements with computer-generated subwavelength gratings. *Opt. Lett.* **27**, 1141-1143

(2002).

38. Saha, S. K. *et al*. Scalable submicrometer additive manufacturing. *Science* **366**, 105-109 (2019).
39. Jin, L. *et al*. Noninterleaved metasurface for (2_6-1) spin- and wavelength-encoded holograms. *Nano Lett.* **18**, 8016-8024 (2018).
40. Huang, C. *et al.* Ultrafast control of vortex microlasers. *Science* **367**, 1018-1021 (2020).
41. Wang, B. *et al.* Generating optical vortex beams by momentum-space polarization vortices centred at bound states in the continuum. *Nat. Photonics* (2020). https://doi.org/10.1038/s41566-020-0658-1.
42. Zhang Z. *et al.* Tunable topological charge vortex microlaser. *Science* **368**, 760-763 (2020).
43. Rivenson, Y., Wu, Y. & Ozcan, A. Deep learning in holography and coherent imaging. *Light Sci. Appl.* **8**, 85 (2019).
44. Grier, D. G. A revolution in optical manipulation. *Nature* **424**, 810-816 (2003).

Acknowledgements: H. R. acknowledges the funding support from the Humboldt Research Fellowship from the Alexander von Humboldt Foundation. S. A. M. acknowledges the funding support from the Deutsche Forschungsgemeinschaft and the Lee-Lucas Chair in Physics. J. R. acknowledges the Samsung Research Funding & Incubation Center for Future Technology grant (SRFC-IT1901-05) funded by Samsung Electronics and the National Research Foundation (NRF) grants (NRF-2019R1A2C3003129, CAMM-2019M3A6B3030637, NRF-2019R1A5A8080290, NRF-2018M3D1A1058997, NRF-2015R1A5A1037668) funded by the Ministry of Science and ICT (MSIT) of the Korean government. J.J. acknowledges the Hyundai Motor *Chung Mong-Koo*

Foundation fellowship, the NRF fellowship (NRF-2019R1A6A3A13091132) funded by the Ministry of Education of the Korean governent, and the NRF-DAAD Summer Institute program funded by the NRF and German Academic Exchange Service (DAAD). X. F. acknowledges the funding support from Shanghai Rising-Star Program (20QA1404100) and Zhangjiang National Innovation Demonstration Zone (ZJ2019-ZD-005).

Author contributions: H. R. and S. A. M. proposed the idea and conceived the experiment; X. F. and H. R. performed the calculation of complex-amplitude OAM-multiplexing holograms; J. J., J. R. and H. R. performed the numerical simulation of 3D meta-atoms; H. R. and J. B. carried out 3D laser printing of large-scale 3D metasurfaces; H. R. and J. B. constructed the optical characterization of metasurface holograms; H. R., J. R., and S. A. M. contributed to the data analysis; all the authors completed the writing of the paper.

Competing interests: The authors declare no competing interests.

Additional Information:

Supplementary Information is available in the online version of the paper.

Reprints and permission information is available online at www.nature.com/repreints.

Correspondence and requests for materials should be addressed to H. R., J. R. or S. A. M.

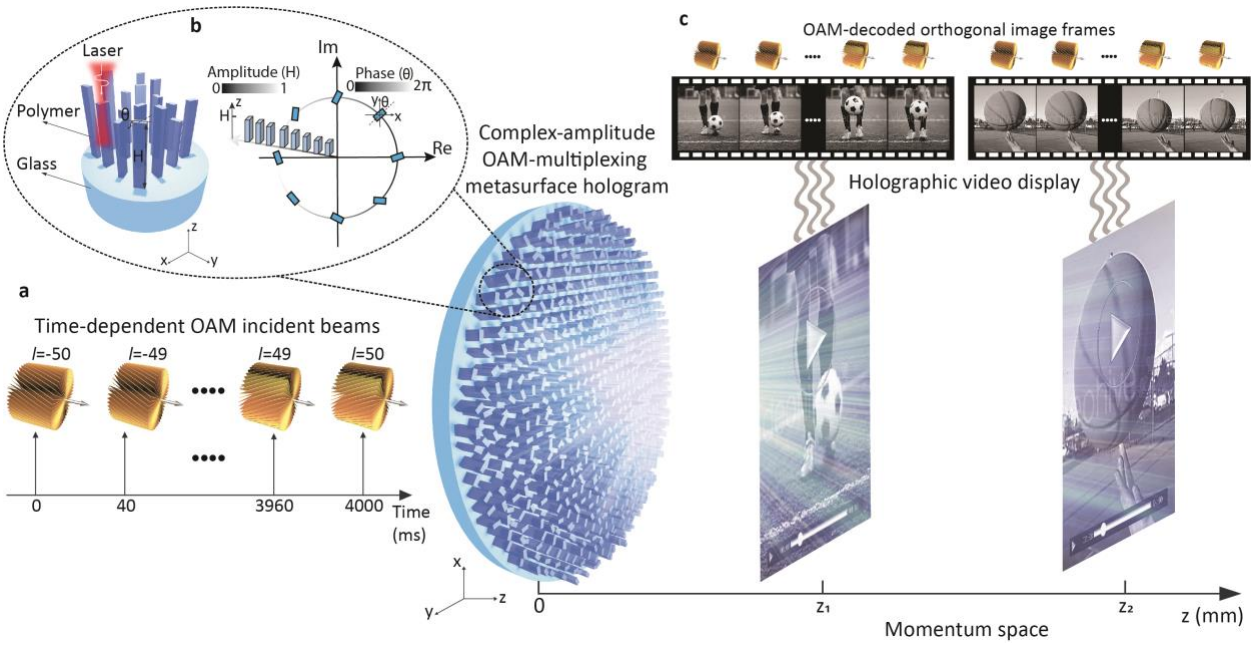

Figure 1. Principle of ultrahigh-dimensional OAM-multiplexing holography based on a large-scale complex-amplitude OAM-multiplexing metasurface hologram**. a**, Time-dependent image frames encoded in an OAM signature with continuous helical mode indices (l) ranging from -50 to 50. **b**, Schematic of an enlarged area of an COMH fabricated by 3D laser printing, in which the out-of-plane height (H) and in-plane rotation (θ) of a birefringent polymer nanopillar offer independent control of both amplitude and phase responses of transmitted light, respectively. **c**, Optically-addressable holographic video display in two image planes (z_1 and z_2) based on a COMH, capable of addressing a large number of OAM-dependent orthogonal image frames in the momentum space of the COMH.

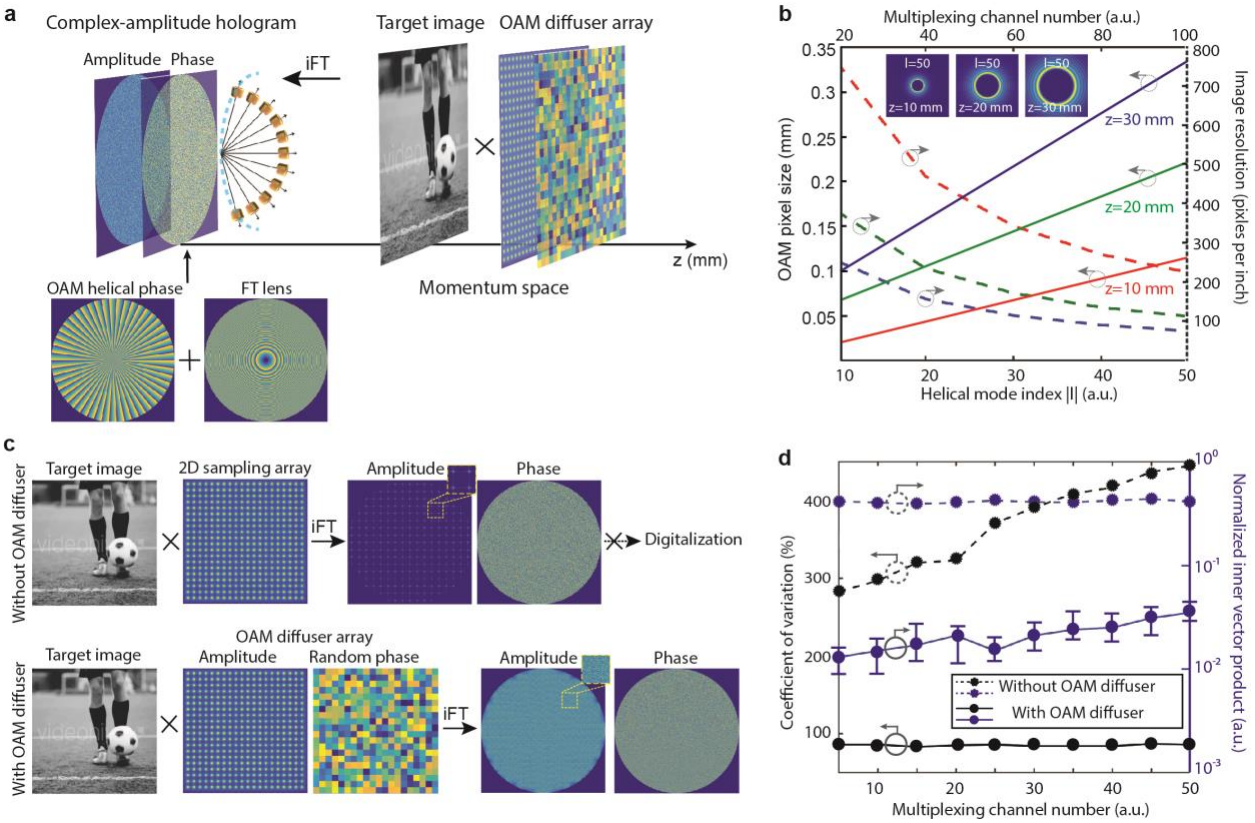

Figure 2. Design principle of a complex-amplitude hologram for OAM holography in momentum space. a, Schematic illustration of OAM holography based on a complex-amplitude hologram that is sampled in its momentum space through an OAM diffuser array. OAM helical phase and a FT lens were added to the phase information of the complex-amplitude hologram, offering strong OAM selectivity at a given image plane. iFT represents inverse Fourier transform. **b**, Numerical characterization of OAM pixel size and image resolution as a function of helical mode index $|l|$ at different image planes, respectively. **c**, The effect of an OAM diffuser array with random phase on the digitalization of a complex-amplitude Fourier hologram. **d**, Numerical characterization of coefficient of variation (black lines) and normalized inner vector product (blue lines) of complex-amplitude Fourier holograms as a function of OAM-multiplexing channel number, with (solid lines) and without (dashed lines) the use of an OAM diffuser array, respectively.

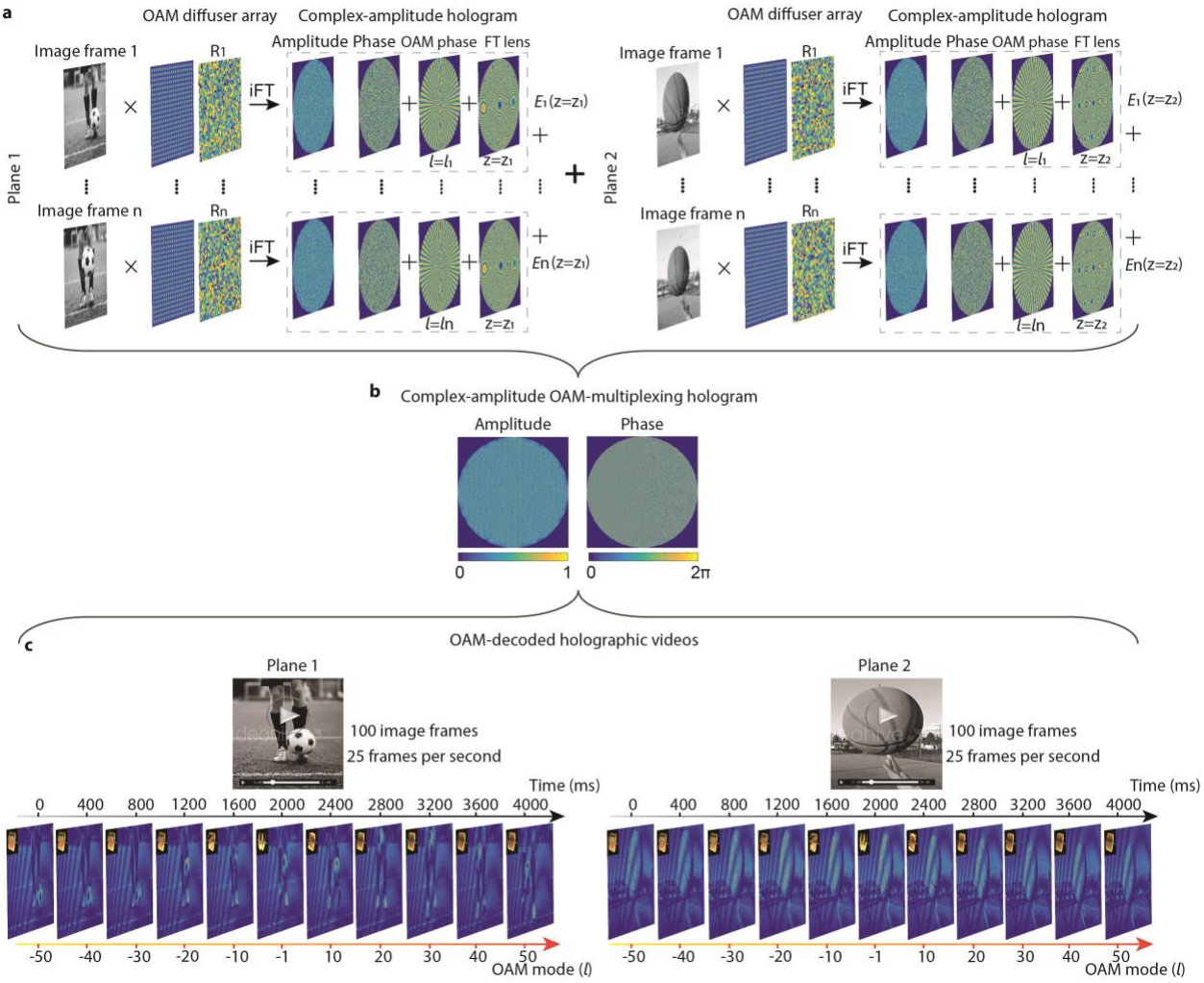

Figure 3. The physical mechanism of complex-amplitude-based OAM-multiplexing holography and its application for a holographic video display. a, The flowchart of designing a complex-amplitude OAM-multiplexing hologram by multiplexing image frames of "football" and "basketball" videos at two image planes, respectively. To calculate a complex-amplitude hologram for each individual image frame, the amplitude of an image frame is multiplied by a complex-valued OAM diffuser array that has a distinct random phase, followed by an inverse Fourier transform. The resultant complex-amplitude hologram further adds an OAM helical phase and a FT lens phase to achieve the OAM selectivity at a given reconstruction distance. Superposition of all the complex-amplitude holograms at different image planes leads to the design of a complex-amplitude OAM-multiplexing hologram. **b**, The designed high-resolution complex-amplitude OAM-multiplexing hologram with 10000 by 10000 pixels. **c**, Numerical demonstration of an all-optical holographic video display based on the designed complex-amplitude OAM-multiplexing hologram in (b), leading to the reconstruction of 100 OAM-dependent holographic image frames in each video.

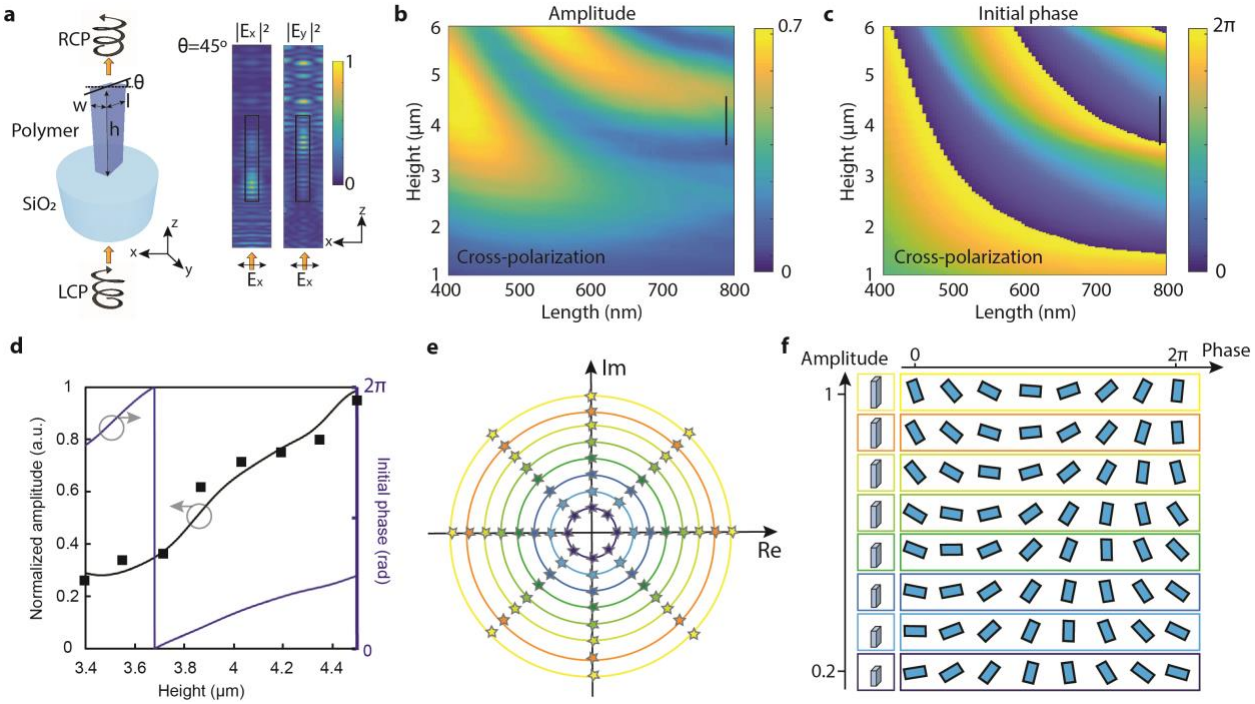

Figure 4. Design and optimization of a 3D metasurface for the complete and independent manipulation of both amplitude and phase responses of transmitted light. a, Schematic of a polymer-based rectangular nanopillar with a high aspect ratio, capable of exhibiting strong birefringence which converts the incident polarization along the x-axis to the one along the y-axis when the nanopillar has a rotation angle of 45 degrees ($\theta = 45^o$) (inset). w, l, h, and θ denote the width, length, height and in-plane rotation angle of a polymer nanopillar. LCP and RCP represent left- and right-handed circular polarization. E_x and E_y represent the linear polarization states along x- and y-axis, respectively. **b** and **c**, Numerical characterization of the amplitude (b) and initial phase retardation (c) of cross polarization transmitted from a nanopillar with different heights (H) and lengths (L), respectively. The black vertical lines in the plots mark the selection of nanopillars to perform amplitude modulation. **d**, Experimental verification of 8-level amplitude modulation through digitalizing a blazed phase grating with selected nanopillars (width: 390 nm and length: 780 nm) of different heights at a wavelength of 633 nm. **e** and **f**, Schematic illustration of 64-level complex-amplitude modulation in the complex plane, based on the selected nanopillars with 8 different heights having 8 different in-plane rotation angles (f).

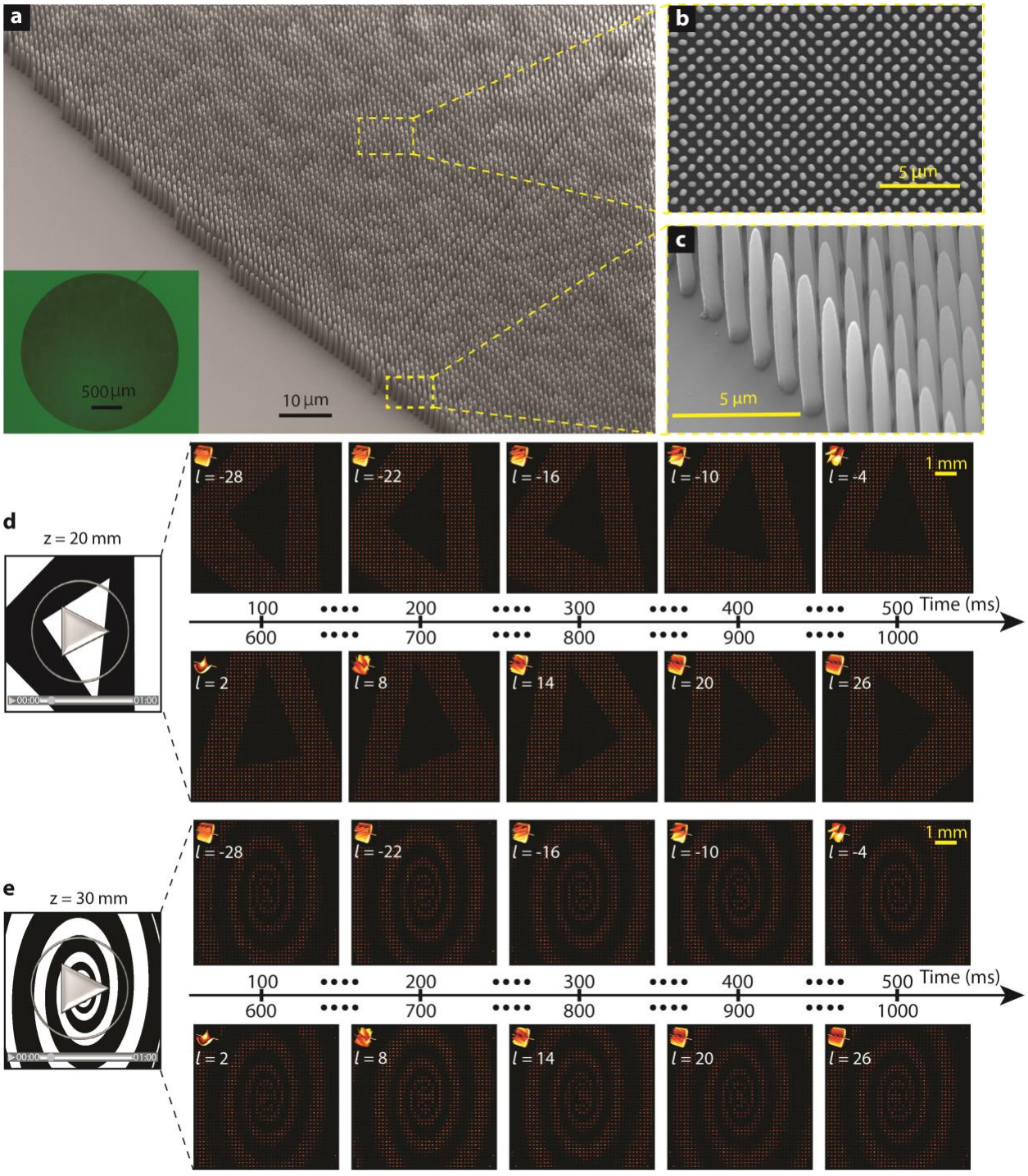

Figure 5. The experimental demonstration of ultrahigh-dimensional OAM-multiplexing holography based on a large-scale complex-amplitude OAM-multiplexing metasurface hologram. a-c, Scanning electron microscope and optical (inset of a) images of a fabricated COMH with a size of 2.5 mm by 2.5 mm, in which the top- (b) and oblique-view (c) scanning electron microscopy images of enlarged areas are presented. **d**, Experimental demonstration of an all-optical holographic video display based on the fabricated COMH in (b), leading to the

reconstruction of 30 OAM-dependent holographic image frames in each video.

Methods

Definition of coefficient of variation. We introduce the coefficient of variation (CV), defined as the ratio of the standard deviation (σ) to the mean (μ) of the amplitude of a complex-amplitude-based Fourier hologram, to compare the variability with and without the OAM diffuser array (Fig. 2d). The CV can be expressed as a dimensionless property $\mathrm{CV} = \sigma/\mu = \sqrt{\frac{1}{(M_X M_Y}\sum\left(AM - \overline{AM}\right)^2}/\overline{AM}$, where AM and $\overline{AM}$ represent the sum of absolute amplitude of the complex-amplitude Fourier hologram and its mean value. M_X and M_Y are the pixel numbers of the hologram along the transverse x- and y-axis, respectively. As a result, a high CV indicates a larger amplitude variation and leads to the failure of digitalization of a complex-amplitude Fourier hologram.

Theoretical and numerical Design and optimization of 3D meta-atoms. Theoretical analysis of polarization conversion efficiency and initial phase of a 3D meta-atom is given in Supplementary Note 3. Numerical simulation of amplitude and phase responses of the 3D meta-atom was carried out by our in-house developed rigorous coupled-wave analysis (RCWA). To provide more physical insights, theoretical and numerical analysis of the transmission coefficients of a nanopillars waveguide is presented in Supplementary Note 4 and fig. S18. The scattering parameters (S-parameters) of a polymer-based meta-atom unit cell with periodic boundary conditions for the polarization along the long transverse axis t_l and the short transverse axis t_S were obtained from the zeroth-order transmission coefficient. According to our analytical results based on Jones matrix calculus, conversion efficiency (square of its amplitude) and initial phase φ_{in} are calculated as

$CE = \left|\frac{t_l - t_s}{2}\right|^2$, $\varphi_{in} = \tan^{-1}(\text{real}\left(\frac{t_l - t_s}{2}\right) / \text{imag}(\left(\frac{t_l - t_s}{2}\right))$, respectively. Commercial COMSOL Multiphysics software was used to evaluate the tapering effect on both the conversion efficiency and initial phase of a 3D meta-atom.

3D laser printing of complex-amplitude metasurface holograms. 3D laser printing of polymer-based complex-amplitude metasurface holograms was realized by two-photon polymerization in a tightly focused femtosecond laser beam. This was done by using a commercial photolithography system (Photonic Professional GT, Nanoscribe GmbH). The polymer metasurface samples were fabricated on ITO-coated soda-lime glass substrates in IP-L 780 resist (Nanoscribe GmbH) by means of a high numerical aperture objective (Plan-Apochromat 63x/1.40 Oil DIC, Zeiss) in the dip-in configuration. The optimized printing parameters were 47.5 mW and 7000 μm/s for laser power and scanning speed, respectively. After laser exposure, the samples were developed by immersion in propylene glycol monomethyl ether acetate (PGMEA, Sigma Aldrich) for 20 minutes, Isopropanol (IPA, Sigma Aldrich) for 5 minutes and Methoxy-nonafluorobutane (Novec 7100 Engineered Fluid, 3M) for 2 minutes. Finally, the fabricated samples were dried in air by evaporation. To increase the mechanical strength of polymer nanopillars with considerably high aspect ratios, a small hatching (laser movement step in the transverse directions: 20 nm) and slicing (laser movement step in the longitudinal direction: 50 nm) distances were employed in our 3D optical printing of complex-amplitude metasurfaces. To significantly increase the fabrication throughput, galvo mirror scanning mode was selected and each scanning field was limited to a square unit cell of 100 μm by 100 μm to reduce the stitching errors and optical aberrations.

Data availability: The data that support the figures and other findings of this study are available

from the corresponding authors upon reasonable request.

Code availability: The code used for the meta-hologram design is available from the corresponding author upon reasonable request.